

Investigating Anisotropic Three-Phonon Interactions in Graphene's Thermal Conductivity Using Monte Carlo Method

Shixian Liu¹, Fei Yin¹, Vladimir I. Khvesyuk^{1*}

¹Department of Thermophysics, Bauman Moscow State Technical University, 2nd Baumanskaya 5, Moscow, 105005, Russian Federation.

*Corresponding author(s). E-mail(s): 2636623@gmail.com;
Contributing authors: sxliu98@gmail.com; yinfei0426@outlook.com;

Abstract

This study introduces a novel method for calculating the thermal conductivity of graphene using a Monte Carlo approach to evaluate anisotropic three-phonon interactions. The phonon dispersion relation is derived using a force constant model that incorporates up to fifth-order nearest-neighbor interactions, while the phonon density of states (DOS) is computed via a generalized Gilat-Raubenheimer method. A quantitative relationship for the scaling exponent of the specific heat capacity at low temperatures is established, emphasizing the unique two-dimensional characteristics of graphene. To address anisotropic effects, the Monte Carlo approach efficiently identifies three-phonon combinations that adhere to the conservation laws of energy and momentum. The findings highlight the pivotal role of anisotropic phonon interactions in graphene's thermal conductivity. The thermal conductivity values obtained through the iterative method exhibit strong agreement with previous three-phonon calculations, thereby validating the model. Nevertheless, discrepancies with experimental data suggest that incorporating higher-order phonon processes, such as four-phonon scattering, may further improve predictive accuracy.

Keywords: Graphene, Density of states, Anisotropic phonon interactions, Monte Carlo method, Thermal conductivity

1 Introduction

Moore's Law predicts that with technological advancements, the number of transistors doubles approximately every 18 to 24 months, leading to enhanced processor performance [1]. However, as transistor sizes shrink below 90 nanometers, overheating becomes a critical issue [2]. The shift from three-dimensional systems to low-dimensional nanosystems fundamentally alters phonon transport, directly impacting heat transfer mechanisms [3–9]. Graphene, a single layer of carbon atoms arranged in a two-dimensional hexagonal lattice, exhibits remarkable electrical [10–12] and thermal [13–15] properties. Experimentally measured thermal conductivity at room temperature ranges from 1000 to 4000 W/mK [16–22], underscoring the challenges in precisely evaluating its thermal performance.

Early calculations of intrinsic lattice thermal conductivity in semiconductors and insulators were based on phonon gas theory using the Boltzmann transport equation (BTE) [23, 24]. The initial thermal conductivity predictions for graphene were also made within this framework. Despite graphene's well-defined structure, unknown interatomic forces and complex phonon-phonon scattering processes complicate accurate predictions of its thermal conductivity. As a result, early models relied on the single-mode relaxation time approximation (RTA) [25–27]. With advancements in computational technology, more rigorous approaches have emerged to calculate graphene's thermal conductivity: (1) determining interatomic forces using empirical potentials [28, 29] or density functional perturbation theory (DFPT) [30–33]; (2) calculating phonon-phonon scattering matrix elements based on anharmonic (third-order or higher) atomic interactions [29, 33].

Software like ShengBTE [34], Fourphonon [35] and Phono3py [36] divide the Brillouin zone into a dense k-space grid, requiring significant computational resources and relying on Gaussian functions to approximate energy and momentum conservation. Our work simplifies these calculations using a Monte Carlo algorithm that accurately identifies phonon combinations satisfying conservation conditions without the need for Gaussian approximation. Previous studies have computed three-phonon N and U processes in silicon and germanium [37], but these assume isotropy. In contrast, graphene's dispersion relations exhibit strong anisotropy, particularly in the high-frequency region. As a result, phonon anisotropy must be integrated into the Monte Carlo algorithm to accurately identify phonon combinations that meet conservation conditions.

This paper proposes a new method for calculating the thermal conductivity of graphene, accounting for anisotropic three-phonon interactions. First, the phonon dispersion relation in the Brillouin zone is constructed using a force constant model [38–40] with up to fifth-nearest neighbors, and the generalized Gilat–Raubenheimer (GGR) [41] method is applied to integrate and numerically solve the density of states (DOS). Next, the specific heat capacity is calculated based on the exact DOS and compared with the Debye model. Finally, the Monte Carlo algorithm is used to find the phonon combination that satisfies the three-phonon interaction conditions, and the phonon relaxation time is determined by combining the scattering matrix calculated by the first principles, and the thermal conductivity of graphene is calculated.

2 Methodology

Fig.1a illustrates the unit cell of graphene, where \mathbf{a}_1 and \mathbf{a}_2 represent the lattice vectors. The lattice constant of graphene is 2.46 Å, and each unit cell contains two atoms. Fig.1b depicts the Brillouin zone in graphene's reciprocal space, with \mathbf{b}_1 and \mathbf{b}_2 as the reciprocal lattice vectors.

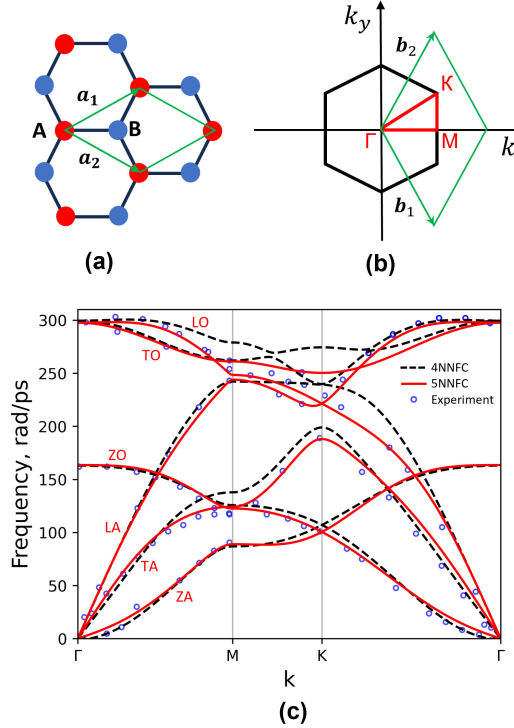


Fig. 1 (a) Graphene unit cell, (b) Brillouin zone representation in k -space, and (c) phonon dispersion relation along the high-symmetry path.

The ionic configuration is characterized by the instantaneous positions of atoms $\mathbf{R}_i(t) = \mathbf{R}_i^0 + \mathbf{u}_i(t)$, where \mathbf{R}_i is the position of the ion at time t , and \mathbf{R}_i^0 is its equilibrium position. The equations of motion are second-order differential equations:

$$M \frac{d^2 \mathbf{u}_i}{dt^2} = \sum_j \Phi^{(i,j)} (\mathbf{u}_j - \mathbf{u}_i), \quad (1)$$

where M is the mass of the atom, and Φ is the force constant tensor. Assuming periodic lattice structure, the solutions take the Bloch wave form

$$\mathbf{u}_i(t) = \mathbf{A} \cdot \exp [i(\mathbf{k} \cdot \mathbf{R}_i^0 - \omega t)], \quad (2)$$

where \mathbf{A} is the mode amplitude, ω is the frequency, and \mathbf{k} is the wave vector. Then, substituting eq.(2) into eq.(1), we obtain the secular equation

$$M\omega^2 \mathbf{A} = D(\mathbf{k}) \cdot \mathbf{A}, \quad (3)$$

where $\omega^2(\mathbf{k})$ is the eigenvalue, $\mathbf{A}(\mathbf{k})$ is the eigenvector, $D(\mathbf{k})$ is a dynamic matrix, which is obtained by the Fourier transform of the force constants taking into account the atoms up to 5th-nearest neighbors [40] referred to as the 5NNFC model. Additionally, the results are compared with those obtained using the 4NNFC model [39]. By solving eq. (3), we obtain six phonon polarization modes (including three acoustic modes and three optical modes). Fig.1c Fig. 1c illustrates the dispersion relation along the high-symmetry path, while Fig. 2a presents the full dispersion relations of the three acoustic modes across the Brillouin zone (BZ).

The effect of anisotropy on the dispersion relation is illustrated in Fig.2a. The sets of closed curves represent lines of constant phonon frequency (energy). Near the center of the Brillouin zone, these curves form closed circles. However, towards the edges of the Brillouin zone, the curves deviate from a circular shape. This indicates that the relationship between frequency and wave vectors depends not only on the magnitude of the vectors but also on their direction.

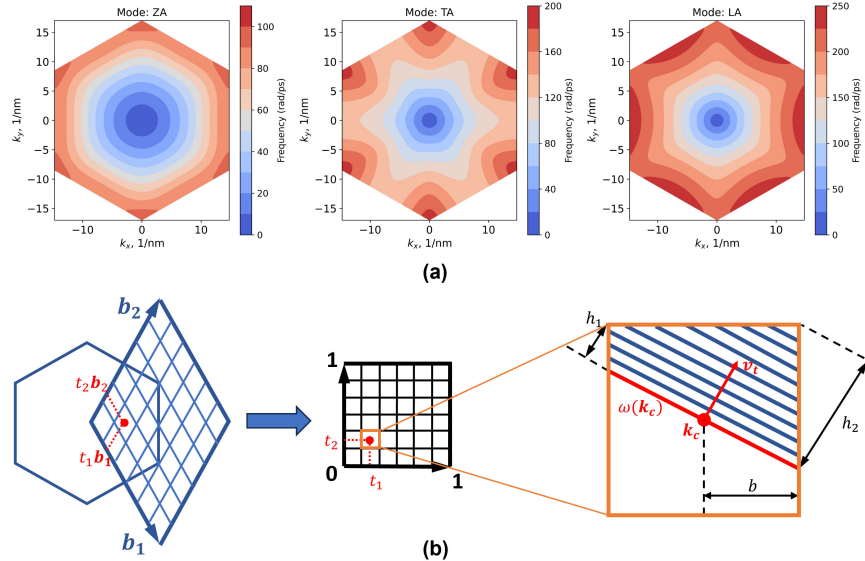


Fig. 2 (a) Full phonon dispersion of graphene in the BZ. (b) General GR method: Linear epitaxy method in the BZ.

The Brillouin zone is a regular hexagon, while the reciprocal lattice is defined by a parallelogram spanned by the reciprocal lattice vectors \mathbf{b}_1 and \mathbf{b}_2 . Despite their differing shapes, the hexagonal Brillouin zone and the parallelogram have equal areas

and share the same frequency distribution, representing the same portion of reciprocal space. Consequently, the integration over the Brillouin zone can be equivalently performed over the parallelogram defined by \mathbf{b}_1 and \mathbf{b}_2 .

As shown in Fig.2b, to calculate the phonon density of states (DOS) in graphene, the GGR method [41] uses an affine transformation to convert the parallelogram defined by the vectors \mathbf{b}_1 and \mathbf{b}_2 into a dimensionless square. The \mathbf{k} points are uniformly distributed along the two basis vectors \mathbf{b}_1 and \mathbf{b}_2 . The affine transformation then maps the \mathbf{k} basis to the $\mathbf{t} = (t_1, t_2)$ basis: $\mathbf{k} = B\mathbf{t} = \mathbf{b}_1t_1 + \mathbf{b}_2t_2$, where $t_1, t_2 \in [0, 1]$ and $B = [\mathbf{b}_1, \mathbf{b}_2]$.

The integral over the parallelogram is transformed into an integral over the square, where $t_1, t_2 \in [0, 1]$. The DOS is then calculated based on $\mathbf{t} = (t_1, t_2)$ using the original Gilat–Rabenheimer (GR) method [42]. The GR method divides the square into uniform small subcells, centered at the coarse grid \mathbf{k}_c -points. Within each subcell, the frequencies in surrounding regions are approximated using linear extrapolation, based on the frequency and group velocity at the center point. The density of states (DOS) is expressed as:

$$\text{DOS}(\omega) = \sum_s g_s(\omega) = \sum_{\mathbf{k}_c, s} \int \frac{dl_{\omega(\mathbf{t})}}{|\mathbf{v}_t|}, \quad (4)$$

where the summation is performed over all cells \mathbf{k}_c and mode indices s , and $l_{\omega(\mathbf{t})}$ represents the length of the isofrequency line for a given frequency ω . In this context, the isofrequency line is represented by segmented lines within each cell [42]. \mathbf{v}_t is obtained by scaling \mathbf{v}_k : $\mathbf{v}_t = \mathbf{v}_k \cdot B = (\mathbf{v}_k \cdot \mathbf{b}_1, \mathbf{v}_k \cdot \mathbf{b}_2) = (\mathbf{v}_{t1}, \mathbf{v}_{t2})$.

Based on the DOS obtained by the GGR method, the heat capacity [43, 44] is calculated:

$$C_v(T) = k_B \sum_s \int_0^{\omega_{s,\max}} \hbar\omega \frac{\partial f^0(\omega, T)}{\partial T} g_s(\omega) d\omega, \quad (5)$$

where f^0 is the Bose-Einstein distribution, k_B is the Boltzmann constant, and T is the temperature.

The steady-state phonon BTE describes the balance of the phonon population between the diffusive drift and the scattering as:

$$-\mathbf{v} \cdot \frac{\partial f^0}{\partial T} \nabla T = \frac{\partial f}{\partial t}|_{\text{scatt}}, \quad (6)$$

where the left-hand side represents the diffusion term, and the right-hand side corresponds to the scattering term. Here, \mathbf{v} is the group velocity, and f is the phonon distribution.

The three-phonon interaction process in crystals is generally divided into two categories: N-process and U-process [44]. The U-process directly impacts thermal resistance, while the N-process does not directly affect thermal resistance but influences thermal conductivity by redistributing phonon modes. Both the N-process and

U-process satisfy the law of energy conservation:

$$\omega_1 \pm \omega_2 = \omega_3, \quad (7)$$

The N-process also satisfies momentum conservation, whereas the U-process violates momentum conservation. However, this violation is compensated by the reciprocal lattice, ensuring the generalized conservation of momentum:

$$\mathbf{k}_1 \pm \mathbf{k}_2 = \mathbf{k}_3, \text{ (N-process)} \quad (8)$$

$$\mathbf{k}_1 \pm \mathbf{k}_2 = \mathbf{k}_3 + \mathbf{G}_i, \quad i = 1, 2, 3, \text{ (U-process)} \quad (9)$$

N-processes preserve the direction of energy flow, as the resulting phonons propagate in the same direction as the combined phonon mode. Consequently, these processes do not contribute to the material's thermal resistance. In contrast, U-processes reverse the direction of energy flow, thereby generating thermal resistance within the material.

Considering both three-phonon scattering and elastic scattering, the scattering term can be expressed as:

$$\frac{\partial f}{\partial t}|_{\text{scatt}} = \frac{\partial f}{\partial t}|_{\text{scatt}}^{3\text{ph}} + \sum_{\text{el}} [(\Psi - \Psi_{\text{el}})\Gamma_{\text{el}}], \quad (10)$$

$$\frac{\partial f}{\partial t}|_{\text{scatt}}^{3\text{ph}} = \sum_{C_+} [(\Psi_1 + \Psi_2 - \Psi_3)\Gamma_{3\text{ph}}^+] + \frac{1}{2} \sum_{C_-} [(\Psi_1 - \Psi_2 - \Psi_3)\Gamma_{3\text{ph}}^-], \quad (11)$$

$$\Gamma_{3\text{ph}}^+ = \frac{\hbar\omega}{4} \frac{f_1^0 - f_3^0}{\omega_1\omega_2\omega_3} |V_{3\text{ph}}^+|, \quad (12)$$

$$\Gamma_{3\text{ph}}^- = \frac{\hbar\omega}{4} \frac{f_1^0 + f_2^0 + 1}{\omega_1\omega_2\omega_3} |V_{3\text{ph}}^-|. \quad (13)$$

Here, $V_{3\text{ph}}^\pm$ denotes the scattering matrix, which is calculated using the `phono3py` program. The summation is performed over the set C_\pm , representing all possible combinations of three phonons that can interact with one another. To satisfy the quasi-momentum conservation condition, the Brillouin zone is discretized into a uniform grid of $N_x \times N_y \times N_z$ points. However, for any specific grid point, most combinations of wave vectors $(\mathbf{k}_1, \mathbf{k}_2, \mathbf{k}_3)$ that satisfy quasi-momentum conservation fail to simultaneously fulfill the energy conservation condition. To simplify the calculation, many studies approximate the delta function with a finite-width function, such as a Gaussian approximation [45, 46].

In this paper, we will determine this set using a Monte Carlo method. Based on the anisotropic phonon dispersion relation in graphene, we can determine the isofrequency lines in \mathbf{k} -space. The vector from the origin to any point on this line represents a possible wave vector for that specific frequency. As shown in the flowchart (Fig.3), for a phonon with frequency ω_1 , the frequency of the second phonon, ω_2 , is determined randomly. According to the law of energy conservation, the frequency of the third phonon is determined by the frequencies of the first two phonons. In the case of the

synthesis process, we have $\omega_3 = \omega_1 + \omega_2$, while for the decomposition process, it is given by $\omega_3 = |\omega_1 - \omega_2|$.

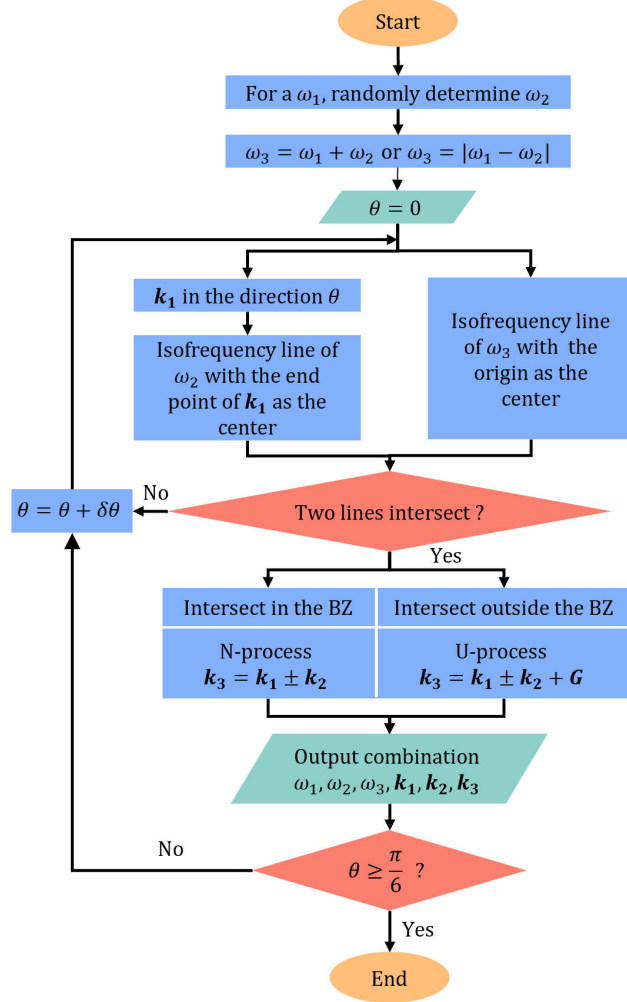


Fig. 3 Flowchart for determining three-phonon combinations based on the Monte Carlo algorithm.

First, assume that the direction of \mathbf{k}_1 is along the positive x-axis, meaning that \mathbf{k}_1 can be uniquely determined based on the frequency ω_1 . If the angle between \mathbf{k}_1 and the x-axis is denoted as θ , then $\theta = 0$. Next, an isofrequency line for ω_2 is drawn with the endpoint of the \mathbf{k}_1 vector as the center. The points on this isofrequency line correspond to the endpoints of the vectors $\mathbf{k}_+ = \mathbf{k}_1 + \mathbf{k}_2$ or $\mathbf{k}_- = \mathbf{k}_1 - \mathbf{k}_2$. Simultaneously, an isofrequency line for ω_3 is drawn centered at the origin. For the U process, it is necessary to draw not only the isofrequency line for ω_3 in the Brillouin zone but also

those outside the Brillouin zone: to the right (Fig.4b), upper right (Fig.4c), and lower right (Fig.4d).

If the curve representing the endpoint of \mathbf{k}_+ or \mathbf{k}_- intersects with the isofrequency line for ω_3 , the combination satisfies the conditions. If the intersection occurs within the first Brillouin zone, it is an N process (Fig.4a). If the intersection occurs outside the first Brillouin zone, it is a U process, and the intersection must be mapped back to the Brillouin zone (i.e., finding an equivalent point in the Brillouin zone) through the reciprocal lattice vectors \mathbf{G}_1 , \mathbf{G}_2 , and \mathbf{G}_3 . These correspond to Fig.4b, 4c, and 4d, respectively.

Finally, the direction of \mathbf{k}_1 is changed, and the angle θ between \mathbf{k}_1 and the x-axis varies within the range $[0, \pi/6]$. The above calculations are repeated to account for not only the anisotropy of the second and third phonons but also the anisotropy of the first phonon.

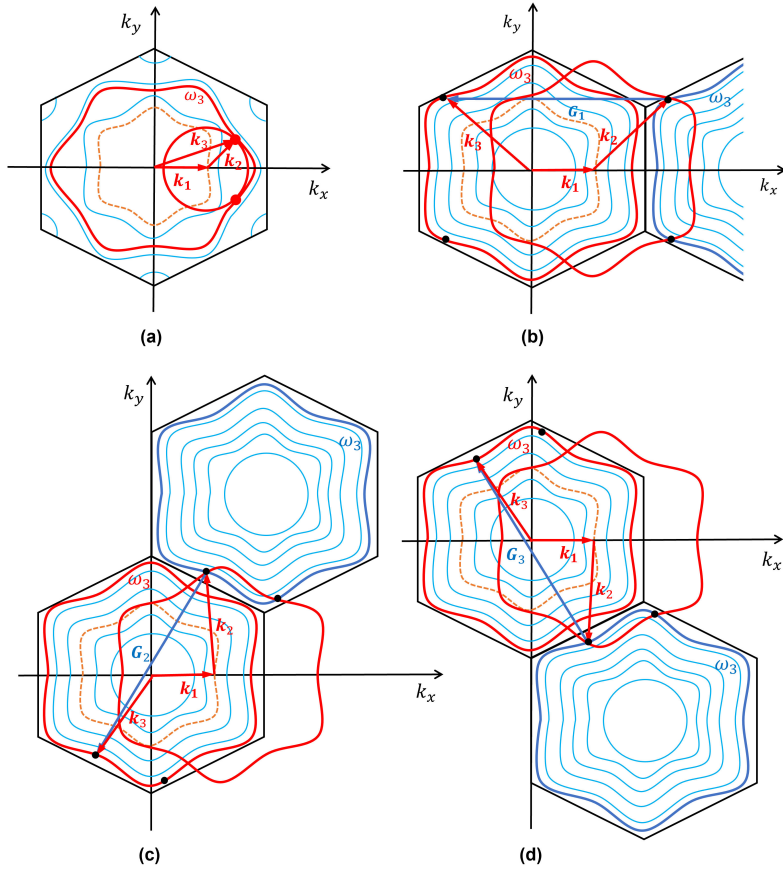


Fig. 4 Schematic diagram of N process and U process when \mathbf{k}_1 is in the direction of x-axis.

The linearized Boltzmann Transport Equation can be expressed in its general form as:

$$\tau_1 = \tau_1^0 + \tau_1^0 \Delta, \quad (14)$$

where the zeroth approximation τ_1^0 is obtained based on the single-mode relaxation time approximation (SMRTA), which assumes $\Psi_2 = \Psi_3 = 0$:

$$\frac{1}{\tau_1^0} = \sum_{C_+} \Gamma_{3\text{ph}}^+ + \frac{1}{2} \sum_{C_-} \Gamma_{3\text{ph}}^- + \sum_{\text{eq}} \Gamma_{\text{el}}. \quad (15)$$

To solve the BTE (14) accurately, the iteration method must be employed, with the homogeneous term Δ given by:

$$\Delta = \sum_{C_+} \Gamma_{3\text{ph}}^+ (\xi_3 \tau_3 - \xi_2 \tau_2) + \frac{1}{2} \sum_{C_-} \Gamma_{3\text{ph}}^- (\xi_3 \tau_3 + \xi_2 \tau_2) + \sum_{\text{eq}} \Gamma_{\text{el}} \xi_{\text{el}} \tau_{\text{el}}. \quad (16)$$

Here, phonons 2 and 3 are accounted for by the terms $\xi_2 = \frac{\omega_2 v_2}{\omega_1 v_1}$ and $\xi_3 = \frac{\omega_3 v_3}{\omega_1 v_1}$.

Once the phonon lifetimes are determined by solving the BTE, the thermal conductivity of graphene can be calculated as [43, 44]:

$$\kappa(T) = k_B \sum_s \int_0^{\omega_{s,\text{max}}} \hbar \omega \frac{\partial f^0(\omega, T)}{\partial T} g_s(\omega) \tau_s(\omega) v_s^2(\omega) d\omega, \quad (17)$$

where the subscript 1 of the phonon lifetime is omitted, and s denotes the phonon polarization.

3 Results and discussion

By randomly calculating different frequency and mode combinations, we can determine the number of intersections and thereby calculate the scattering probabilities for both the N-process and U-process. (Some model combinations of calculations are given in the supplementary material.) Due to graphene's single-atom-layer structure, its Hamiltonian exhibits invariance along the z-axis, a consequence of its planar symmetry. This structural symmetry imposes specific selection rules on phonon interactions, particularly for out-of-plane acoustic (ZA) phonons, which are responsible for flexural vibrations. One key result of this symmetry is that three-phonon scattering processes involving ZA phonons are restricted: only processes involving an even number of ZA phonons are allowed. For example, allowed processes include ZA + ZA = LA, ZA + ZA = TA, LA + ZA = ZA, and TA + ZA = ZA. Conversely, processes involving an odd number of ZA phonons, such as ZA + LA = TA, are prohibited by this selection rule.

This limitation has important implications for phonon transport in graphene. ZA phonons have long wavelengths and they contribute significantly to thermal conduction. However, since the odd ZA scattering process is prohibited, the scattering rate

of the ZA mode is low, resulting in a long relaxation time for the ZA mode. This will lead to high thermal conductivity in graphene. Although in subsequent studies of the four-phonon process, the ZA mode will be scattered more, reducing the relaxation time, thereby reducing the thermal conductivity of graphene.

Fig.5 shows the frequency dependence of the scattering rates of these processes in different phonon branches. There are significant differences between the N process and the U process. The N process maintains the total phonon momentum and redistributes energy primarily between phonons without increasing the total thermal resistance. The process tends to dominate at low frequencies, when the phonon interaction energy is low and thermal conduction is more efficient. In contrast, the U process transfers phonon momentum to the lattice, violating momentum conservation and directly increasing thermal resistance. In the SMRTA framework, the N process and the U process are treated as independent scattering events. Using the Matthiessen rule, SMRTA calculates the total relaxation time as $\tau^{-1} = \tau_N^{-1} + \tau_U^{-1}$, which overlooks the fact that the N process does not directly impact thermal resistance. However, in three-phonon scattering, the N process and the U process are inherently coupled. To address this, the phonon distribution function is refined iteratively, allowing it to dynamically adapt to the intricate scattering processes and accurately determine the total scattering rate.

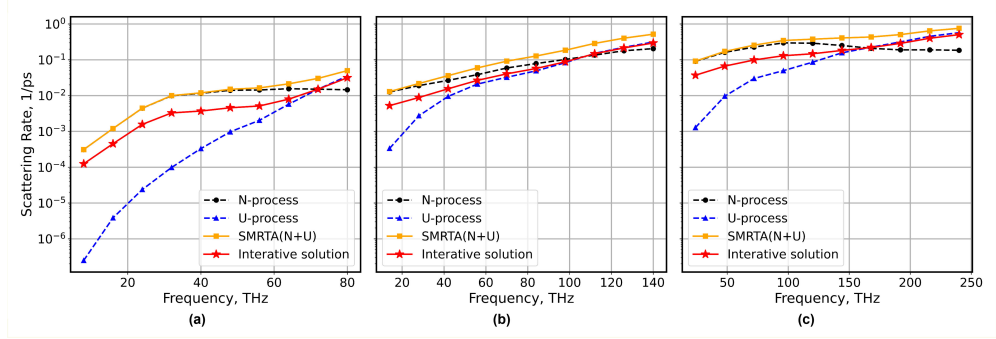


Fig. 5 The frequency dependence of the scattering rates of these processes for (a) ZA branch, (b) TA branch, and (c) LA branch. The figure compares the scattering rates of the N process and U process, the total scattering rate calculated using the Matthiessen rule, and the total scattering rate obtained via the iterative method.

Fig.6a shows the phonon density of states (DOS) of graphene obtained using the GGR method, while Fig.6b presents the specific heat capacity calculated from this density of states. We compare these results with the widely used Debye model, which is commonly employed to describe the specific heat capacity of solids. At high temperatures, both models show good agreement. However, a clear deviation occurs at low temperatures. The Debye model assumes a linear dispersion relation for acoustic phonons and a quadratic relation for the DOS, predicting a T^3 dependence [47] of the specific heat capacity at low temperatures—a relationship well-established in three-dimensional systems.

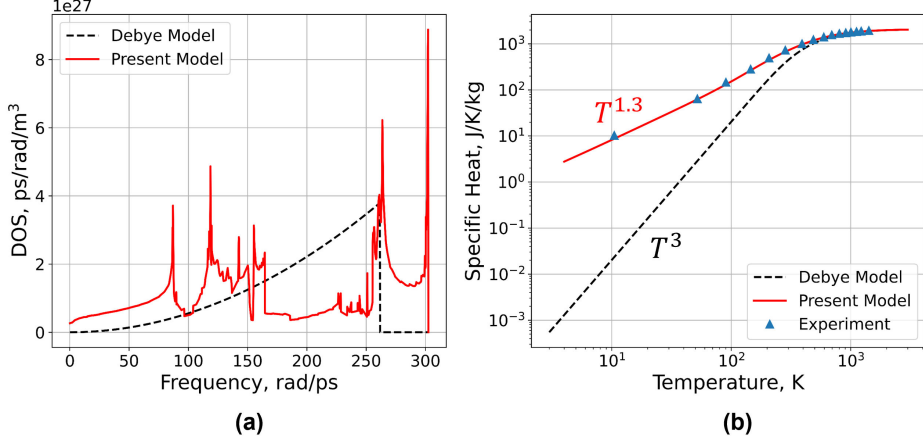


Fig. 6 (a) Phonon DOS and (b) specific heat capacity of graphene: The results of the current model are shown with a solid red line, and the Debye model with a dashed black line. The blue filled triangles are experimental values [48].

In contrast, our results reveal a different low-temperature behavior based on the actual phonon DOS in graphene, exhibiting a $T^{1.3}$ dependence. This deviation can be attributed to graphene's unique two-dimensional structure, which significantly alters its phonon spectrum, particularly for out-of-plane acoustic (ZA) phonons that contribute substantially to the heat capacity at low temperatures. This finding is important, as many low-dimensional systems or nanostructures exhibit complex phonon spectra and DOS, where the bending modes of low-dimensional systems and the quantum confinement effects of nanostructures have a significant impact on the temperature dependence of the specific heat capacity.

This result is consistent with previous research findings [49, 50]. Considering the constraints of dimensionality, existing studies have shown that the specific heat capacity of a one-dimensional system is linearly related to temperature at low temperatures, $C_{1D} \sim T$, while the specific heat capacity of a two-dimensional system is quadratically related to temperature, $C_{2D} \sim T^2$. However, these results are based on the assumption of a linear dispersion relation, $\omega \sim k$. In the case of graphene, the out-of-plane bending mode exhibits a quadratic dispersion relation, $\omega \sim k^2$. This leads to a different density of states distribution and results in the specific heat capacity following the relationship $C \sim T^{1.3}$.

Fig. 7a and Fig. 7b show the thermal conductivity results based on the SMRTA framework and the thermal conductivity results based on the iterative method, respectively. Although we aim to perform gridless computations, we still introduce a uniform angular division, $\theta = \theta + \delta\theta$. This is primarily to account for the anisotropy in graphene's dispersion relations. For isotropic materials such as silicon or germanium, gridless computation is feasible. Even with this adjustment, our grid remains one-dimensional, denoted as N_θ , as illustrated in Fig. 7a and Fig. 7b. Typically, $N_\theta = 60$ is sufficient to achieve convergence. This represents a significant reduction compared to the two-dimensional or three-dimensional grids required in earlier approaches.

In Fig. 7a and Fig. 7b, $N_\theta = 1$, which assumes that phonon 1 is isotropic. This assumption leads to an overestimation of thermal conductivity in highly anisotropic materials such as graphene. As N_θ increases, more anisotropic scattering is accounted for, resulting in the gradual convergence of thermal conductivity.

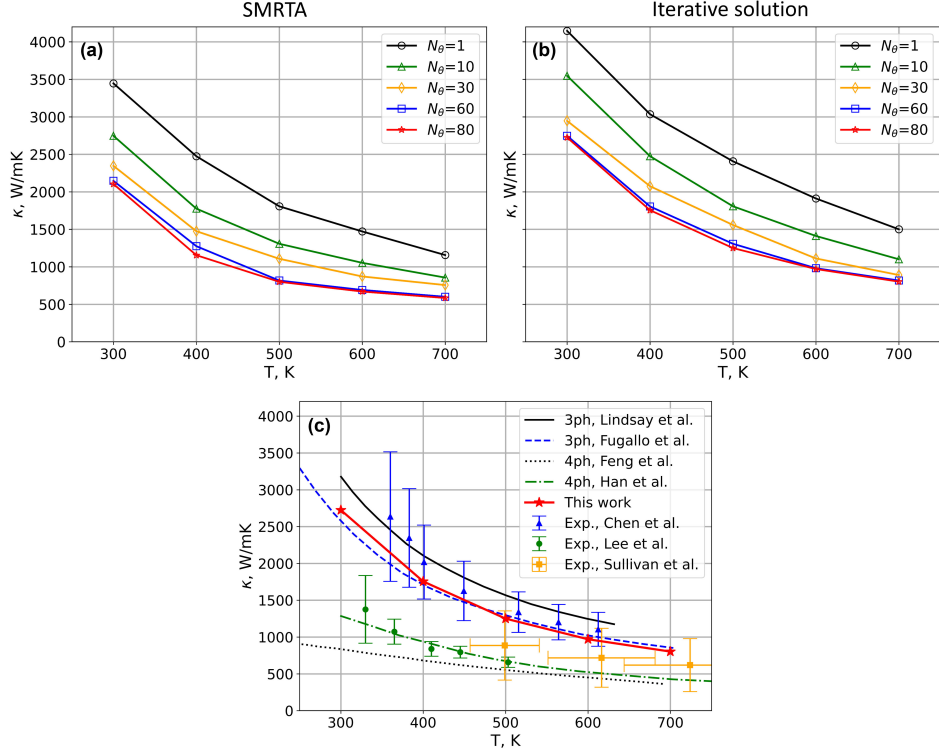


Fig. 7 (a) Convergence of thermal conductivity with respect to the angular grid number calculated using the SMRTA method, (b) Convergence of thermal conductivity with respect to the angular grid number calculated using the iterative method, and (c) Thermal conductivity of graphene as a function of temperature. Our results calculated using the iterative method are shown as solid red lines with filled circles. The first-principles calculation results considering three-phonon interactions are shown as black solid line [30] and blue dashed line [31]. The calculation results based on Tersoff potential and considering four-phonon interaction and the calculation results based on DFT considering four-phonon interaction are shown as black dotted lines [29] and green dot-dashed lines [35], respectively. The three sets of experimental data are shown as blue filled triangles [19], green filled circles [20], and orange filled squares [22], respectively.

To facilitate comparison with experimental and calculated data, we present the temperature dependence of graphene's thermal conductivity in Fig. 7c. The significant uncertainties associated with experimental measurements using Raman techniques [19] (solid triangles) and [20] (solid circles) pose challenges for validating predictions from both this work and prior studies. Additionally, we include experimental data obtained

using an improved optical measurement method [22] (yellow squares). Our calculations demonstrate close agreement with these experimental results, with discrepancies primarily arising from the exclusion of higher-order phonon scattering in our model.

We also compare our results with previous three-phonon calculations based on DFT theory [30][31]. By explicitly distinguishing between N and U processes, we accurately evaluate their individual contributions to the total scattering rate. This evaluation is performed not only under the SMRTA approximation but also through an iterative method that couples these processes. Furthermore, our Monte Carlo approach to three-phonon interactions eliminates the need for a fixed k-space grid, allowing for a precise assessment of possible phonon states while significantly reducing computational complexity. Notably, the results from our iterative method align closely with those of three-phonon calculations based on DFT [31], validating the accuracy of our model.

Finally, we incorporate results from Ruan's group's four-phonon scattering calculations, based on both the Tersoff potential [29] and DFT [35]. These findings highlight the critical role of higher-order scattering effects, which are consistent with Lee's experimental data, though they remain below the most recent experimental observations.

4 Conclusion

In this study, we developed an advanced method to calculate the thermal conductivity of graphene by integrating anisotropic three-phonon interactions with the Monte Carlo approach. We introduce a new quantitative determination of the specific heat capacity scaling exponent ($T^{1.3}$) for graphene at low temperatures, capturing its distinctive two-dimensional characteristics. Our findings underscore the pivotal role of anisotropic phonon interactions in thermal transport. By examining phonon behavior at varying angles, we compared anisotropic and isotropic results, revealing the significant influence of angular dependence on thermal conductivity. Furthermore, the thermal conductivity values obtained using the iterative method demonstrate strong agreement with previous three-phonon calculations, further validating our model.

The Monte Carlo approach enabled the precise identification of phonon triplet combinations that satisfy energy and momentum conservation, eliminating the reliance on a fixed k-space grid. This flexibility facilitated a detailed analysis of three-phonon interactions, including their contributions to scattering rates and relaxation times. Nonetheless, slight discrepancies between our results and experimental data suggest the necessity of incorporating higher-order phonon processes, such as four-phonon scattering, in future studies to enhance the accuracy of thermal conductivity predictions.

Acknowledgements. S. Liu and F. Yin gratefully acknowledge financial support from the China Scholarship Council.

Declarations

- **Funding** This work is supported by the China Scholarship Council (Grant No. 202308090243 for S. Liu and Grant No. 202408090635 for F. Yin).
- **Conflict of interest** The authors declare no competing interests.
- **Author Contributions** S. Liu: Investigation, Methodology, Writing—original draft, Visualization. F. Yin: Methodology, Formal analysis, Writing—review & editing. V.I. Khvesyuk Conceptualization, Methodology, Supervision, Writing—review & editing.

Appendix A Nearest Neighbor Force Constant Model

The force constant model used consists of a direct parameterization of the diagonal real-space force constants, including the 4NNFC method up to the fourth nearest neighbor interaction and the 5NNFC method up to the fifth nearest neighbor interaction. The force constant tensor describes the interaction between an atom and its n th nearest neighbor on an arbitrarily chosen axis, e.g., has the diagonal form on the x -axis:

$$\Phi^{(n)} = \begin{pmatrix} \phi_r^{(n)} & 0 & 0 \\ 0 & \phi_{ti}^{(n)} & 0 \\ 0 & 0 & \phi_{to}^{(n)} \end{pmatrix}, \quad (\text{A1})$$

where $\phi_r^{(n)}$, $\phi_{ti}^{(n)}$, and $\phi_{to}^{(n)}$ represent the force-constant parameters in the radial bond-stretching, in-plane, and out-of-plane tangential bond-bending directions of the n th-nearest neighbors. The radial direction corresponds to the direction of the bonds and the two tangential directions are perpendicular to it, as illustrated in Fig. A1. These parameters are listed in Table A1.

The force-constant tensors for nearest-neighbor atoms of the same neighbor shell, which are not located on the x axis, can be obtained by unitary rotation of the tensor in Eq.(A1). A unitary rotation matrix around the z -axis is

$$U_z(\theta) = \begin{pmatrix} \cos(\theta) & \sin(\theta) & 0 \\ -\sin(\theta) & \cos(\theta) & 0 \\ 0 & 0 & 1 \end{pmatrix}. \quad (\text{A2})$$

where, θ is the angle between the atomic stretching and the x -axis.

For example, for first-nearest neighbors $n = 1$, we obtain the force-constant tensor between atom A0 and its first nearest-neighbor atoms B0, B1, B2:

$$\Phi(A_0, B_0) = \Phi^{(n=1)} \quad (\text{A3})$$

$$\Phi(A_0, B_1) = U_z^{-1}(2\pi/3)\Phi^{(n=1)}U_z(2\pi/3) \quad (\text{A4})$$

$$\Phi(A_0, B_2) = U_z^{-1}(4\pi/3)\Phi^{(n=1)}U_z(4\pi/3) \quad (\text{A5})$$

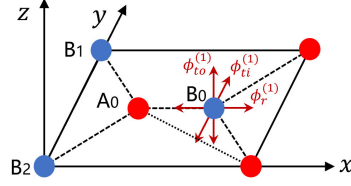


Fig. A1 Atom A0 and its first nearest-neighbor atoms B0, B1, B2.

Table A1 Parameters of the force constant model (4NNFC and 5NNFC) for graphene, N/m

Neighbor shell	4NNFC ¹			5NNFC ²		
	$\phi_r^{(n)}$	$\phi_{ti}^{(n)}$	$\phi_{to}^{(n)}$	$\phi_r^{(n)}$	$\phi_{ti}^{(n)}$	$\phi_{to}^{(n)}$
$n = 1$	365.0	245.0	98.2	414.644	134.903	99.063
$n = 2$	88.0	-32.3	-4.0	64.680	-48.770	-7.883
$n = 3$	30.0	-52.5	1.5	-48.322	63.254	8.267
$n = 4$	-19.2	22.9	-5.8	9.036	2.067	-8.347
$n = 5$	-	-	-	16.582	2.660	1.762

¹Parameters for model 4NNFC from [39].

²Parameters for model 5NNFC from [40].

Appendix B Examples of three-phonon process combinations

As shown in Fig. B2, the modes and frequencies of two phonons are used as input. Through the conservation of energy, the frequency of the third phonon can be determined. The mode of the third phonon is randomly assigned. Subsequently, the wave vectors corresponding to the three phonons, as well as the proportion of the N process and U process are determined based on the conservation of momentum.

The yellow line represents the isofrequency line for ω_1 . All points on this line may correspond to the endpoint of the wave vector \mathbf{k}_1 . To illustrate symmetry, we plot the angle θ between \mathbf{k}_1 and the x-axis, ranging from $-\pi/6$ to $\pi/6$. In fact, due to symmetry, the intervals $-\pi/6$ to 0 and 0 to $\pi/6$ contain equivalent information.

The blue line is the isofrequency line for ω_2 , drawn with the endpoint of \mathbf{k}_1 as its center. Points on this line represent the possible endpoints of the vector $\mathbf{k}_1 + \mathbf{k}_2$. The red line indicates the isofrequency line for ω_3 , centered at the origin of the Brillouin zone. Points on this line correspond to the possible endpoints of the wave vector \mathbf{k}_3 . If the red line intersects the solid blue line, the intersection signifies a three-phonon mode combination that may lead to the N process.

Furthermore, if a portion of the blue line extends beyond the Brillouin zone, a reciprocal lattice vector \mathbf{G}_i ($i = 1, 2, 3$) is subtracted from all points on the blue line to obtain a new curve. The points on this new curve correspond to the vector $\mathbf{k}_1 + \mathbf{k}_2 - \mathbf{G}_i$. If this new curve intersects the red line within the Brillouin zone,

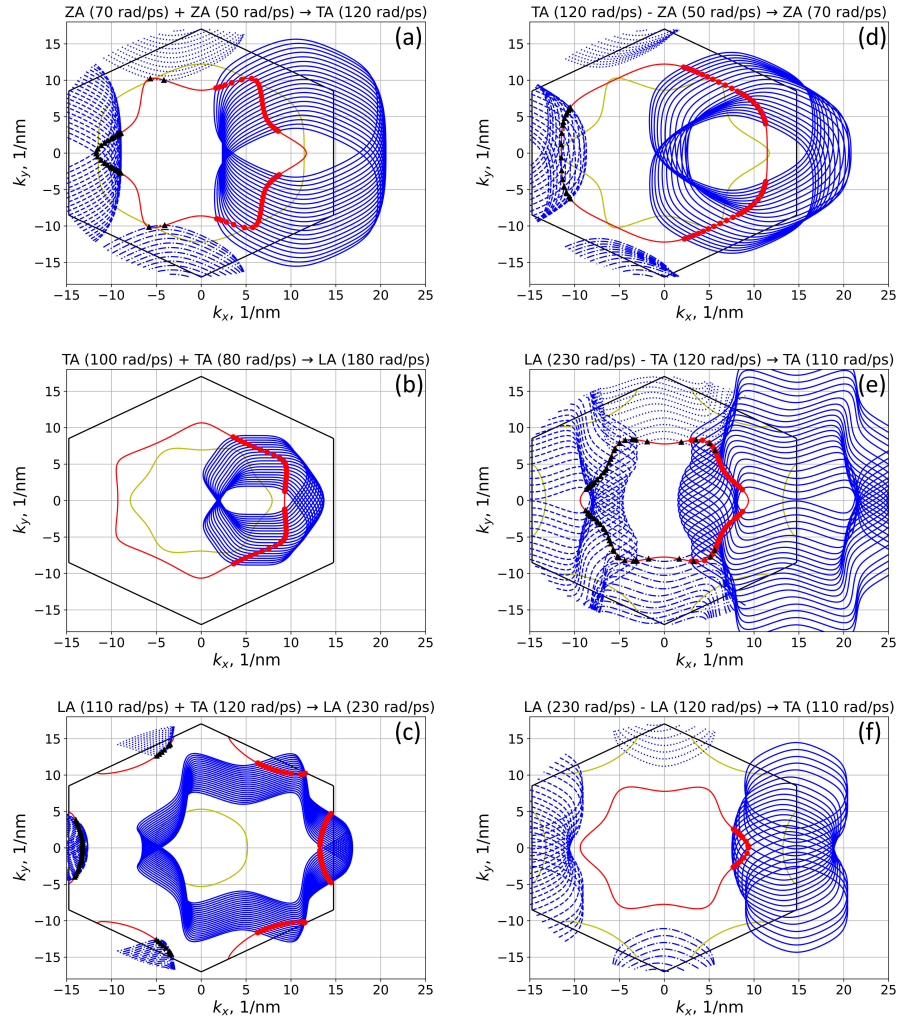


Fig. B2 Two phonons combine to create a phonon: (a) ZA+ZA=TA, (b)TA+TA=LA, (c)LA+TA=LA; One phonon splits into two phonons: (d)TA=ZA+ZA, (e)LA=TA+TA, (f)LA=LA+TA.

the intersection indicates a three-phonon mode combination that may lead to the *U* process. The following are some typical examples of the calculation results.

By randomly generating different combinations of frequencies and modes, we can determine the number of intersections, which allows us to calculate the scattering probabilities for both the *N*-process and *U*-process.

References

- [1] Moore, G.E.: Cramming more components onto integrated circuits. IEEE Solid-State Circuits Society Newsletter **11**(3), 33–35 (2006) <https://doi.org/10.1109/N-SSC.2006.4785860>
- [2] Waldrop, M.M.: The chips are down for Moore’s law. Nature News **530**(7589), 144 (2016) <https://doi.org/10.1038/530144a>
- [3] Cahill, D.G., Ford, W.K., Goodson, K.E., Mahan, G.D., Majumdar, A., Maris, H.J., Merlin, R., Phillpot, S.R.: Nanoscale thermal transport. Journal of Applied Physics **93**(2), 793–818 (2003) <https://doi.org/10.1063/1.1524305>
- [4] Yang, N., Zhang, G., Li, B.: Violation of Fourier’s law and anomalous heat diffusion in silicon nanowires. Nano Today **5**(2), 85–90 (2010) <https://doi.org/10.1016/j.nantod.2010.02.002>
- [5] Maldovan, M.: Micro to nano scale thermal energy conduction in semiconductor thin films. Journal of Applied Physics **110**(3), 034308 (2011) <https://doi.org/10.1063/1.3607295>
- [6] Lim, J., Hippalgaonkar, K., Andrews, S.C., Majumdar, A., Yang, P.: Quantifying Surface Roughness Effects on Phonon Transport in Silicon Nanowires. Nano Lett **12**(5), 2475–2482 (2012) <https://doi.org/10.1021/nl3005868>
- [7] Zeng, Y.-J., Liu, Y.-Y., Zhou, W.-X., Chen, K.-Q.: Nanoscale thermal transport: Theoretical method and application. Chinese Phys. B **27**(3), 036304 (2018) <https://doi.org/10.1088/1674-1056/27/3/036304>
- [8] Taniguchi, T., Terada, T., Komatsubara, Y., Ishibe, T., Konoike, K., Sanada, A., Naruse, N., Mera, Y., Nakamura, Y.: Phonon transport in the nano-system of Si and SiGe films with Ge nanodots and approach to ultralow thermal conductivity. Nanoscale **13**(9), 4971–4977 (2021) <https://doi.org/10.1039/D0NR08499A>
- [9] Liu, S., Barinov, A.A., Yin, F., Khvesyuk, V.I.: Determination of thermal properties of unsmooth Si-nanowires. Chinese Phys. Lett. **41**, 016301 (2024)
- [10] Novoselov, K.S., Geim, A.K., Morozov, S.V., Jiang, D., Katsnelson, M.I., Grigorieva, I.V., Dubonos, S.V., Firsov, A.A.: Two-dimensional gas of massless Dirac fermions in graphene. Nature **438**(7065), 197–200 (2005) <https://doi.org/10.1038/nature04233>
- [11] Zhang, Y., Tan, Y.-W., Stormer, H.L., Kim, P.: Experimental observation of the quantum Hall effect and Berry’s phase in graphene. Nature **438**(7065), 201–204 (2005) <https://doi.org/10.1038/nature04235>
- [12] Son, Y.-W., Cohen, M.L., Louie, S.G.: Half-metallic graphene nanoribbons.

- Nature **444**(7117), 347–349 (2006) <https://doi.org/10.1038/nature05180>
- [13] Ghosh, S., Bao, W., Nika, D.L., Subrina, S., Pokatilov, E.P., Lau, C.N., Balandin, A.A.: Dimensional crossover of thermal transport in few-layer graphene. Nature Mater **9**(7), 555–558 (2010) <https://doi.org/10.1038/nmat2753>
 - [14] Prasher, R.: Graphene Spreads the Heat. Science **328**(5975), 185–186 (2010) <https://doi.org/10.1126/science.1188998>
 - [15] Ren, W., Cheng, H.-M.: The global growth of graphene. Nature Nanotech **9**(10), 726–730 (2014) <https://doi.org/10.1038/nnano.2014.229>
 - [16] Balandin, A.A., Ghosh, S., Bao, W., Calizo, I., Teweldebrhan, D., Miao, F., Lau, C.N.: Superior Thermal Conductivity of Single-Layer Graphene. Nano Lett. **8**(3), 902–907 (2008) <https://doi.org/10.1021/nl0731872>
 - [17] Ghosh, S., Calizo, I., Teweldebrhan, D., Pokatilov, E.P., Nika, D.L., Balandin, A.A., Bao, W., Miao, F., Lau, C.N.: Extremely high thermal conductivity of graphene: Prospects for thermal management applications in nanoelectronic circuits. Appl. Phys. Lett. **92**(15), 151911 (2008) <https://doi.org/10.1063/1.2907977>
 - [18] Cai, W., Moore, A.L., Zhu, Y., Li, X., Chen, S., Shi, L., Ruoff, R.S.: Thermal Transport in Suspended and Supported Monolayer Graphene Grown by Chemical Vapor Deposition. Nano Lett. **10**(5), 1645–1651 (2010) <https://doi.org/10.1021/nl9041966>
 - [19] Chen, S., Moore, A.L., Cai, W., Suk, J.W., An, J., Mishra, C., Amos, C., Magnuson, C.W., Kang, J., Shi, L., Ruoff, R.S.: Raman Measurements of Thermal Transport in Suspended Monolayer Graphene of Variable Sizes in Vacuum and Gaseous Environments. ACS Nano **5**(1), 321–328 (2011) <https://doi.org/10.1021/nn102915x>
 - [20] Lee, J.-U., Yoon, D., Kim, H., Lee, S.W., Cheong, H.: Thermal conductivity of suspended pristine graphene measured by Raman spectroscopy. Phys. Rev. B **83**(8), 081419 (2011) <https://doi.org/10.1103/PhysRevB.83.081419>
 - [21] Xu, X., Pereira, L.F.C., Wang, Y., Wu, J., Zhang, K., Zhao, X., Bae, S., Tinh Bui, C., Xie, R., Thong, J.T.L., Hong, B.H., Loh, K.P., Donadio, D., Li, B., Özyilmaz, B.: Length-dependent thermal conductivity in suspended single-layer graphene. Nat Commun **5**(1), 3689 (2014) <https://doi.org/10.1038/ncomms4689>
 - [22] Sullivan, S., Vallabhaneni, A., Kholmanov, I., Ruan, X., Murthy, J., Shi, L.: Optical Generation and Detection of Local Nonequilibrium Phonons in Suspended Graphene. Nano Lett. **17**(3), 2049–2056 (2017) <https://doi.org/10.1021/acs.nanolett.7b00110>

- [23] Callaway, J.: Model for Lattice Thermal Conductivity at Low Temperatures. *Phys. Rev.* **113**(4), 1046–1051 (1959) <https://doi.org/10.1103/PhysRev.113.1046>
- [24] Holland, M.G.: Analysis of Lattice Thermal Conductivity. *Phys. Rev.* **132**(6), 2461–2471 (1963) <https://doi.org/10.1103/PhysRev.132.2461>
- [25] Nika, D.L., Ghosh, S., Pokatilov, E.P., Balandin, A.A.: Lattice thermal conductivity of graphene flakes: Comparison with bulk graphite. *Appl. Phys. Lett.* **94**(20), 203103 (2009) <https://doi.org/10.1063/1.3136860>
- [26] Alofi, A., Srivastava, G.P.: Thermal conductivity of graphene and graphite. *Phys. Rev. B* **87**(11), 115421 (2013) <https://doi.org/10.1103/PhysRevB.87.115421>
- [27] Alofi, A., Srivastava, G.P.: Evolution of thermal properties from graphene to graphite. *Appl. Phys. Lett.* **104**(3), 031903 (2014) <https://doi.org/10.1063/1.4862319>
- [28] Hou, X.H., Deng, Z.C., Zhang, K.: A structural mechanics approach for the phonon dispersion analysis of graphene. *Physica E: Low-dimensional Systems and Nanostructures* **88**, 252–258 (2017) <https://doi.org/10.1016/j.physe.2017.01.012>
- [29] Feng, T., Ruan, X.: Four-phonon scattering reduces intrinsic thermal conductivity of graphene and the contributions from flexural phonons. *Phys. Rev. B* **97**(4), 045202 (2018) <https://doi.org/10.1103/PhysRevB.97.045202>
- [30] Lindsay, L., Li, W., Carrete, J., Mingo, N., Broido, D.A., Reinecke, T.L.: Phonon thermal transport in strained and unstrained graphene from first principles. *Phys. Rev. B* **89**(15), 155426 (2014) <https://doi.org/10.1103/PhysRevB.89.155426>
- [31] Fugallo, G., Cepellotti, A., Paulatto, L., Lazzeri, M., Marzari, N., Mauri, F.: Thermal Conductivity of Graphene and Graphite: Collective Excitations and Mean Free Paths. *Nano Lett.* **14**(11), 6109–6114 (2014) <https://doi.org/10.1021/nl502059f>
- [32] Sohier, T., Calandra, M., Mauri, F.: Density functional perturbation theory for gated two-dimensional heterostructures: Theoretical developments and application to flexural phonons in graphene. *Phys. Rev. B* **96**(7), 075448 (2017) <https://doi.org/10.1103/PhysRevB.96.075448>
- [33] Han, Z., Ruan, X.: Thermal conductivity of monolayer graphene: Convergent and lower than diamond. *Phys. Rev. B* **108**(12), 121412 (2023) <https://doi.org/10.1103/PhysRevB.108.L121412>
- [34] Li, W., Carrete, J., A. Katcho, N., Mingo, N.: ShengBTE: A solver of the Boltzmann transport equation for phonons. *Computer Physics Communications* **185**(6), 1747–1758 (2014) <https://doi.org/10.1016/j.cpc.2014.02.015>

- [35] Han, Z., Yang, X., Li, W., Feng, T., Ruan, X.: FourPhonon: An extension module to ShengBTE for computing four-phonon scattering rates and thermal conductivity. *Computer Physics Communications* **270**, 108179 (2022) <https://doi.org/10.1016/j.cpc.2021.108179>
- [36] Togo, A.: First-principles Phonon Calculations with Phonopy and Phono3py. *J. Phys. Soc. Jpn.* **92**(1), 012001 (2023) <https://doi.org/10.7566/JPSJ.92.012001>
- [37] Khvesyuk, V.I., Barinov, A.A., Liu, B., Qiao, W.: Fundamentally New Approaches for Solving Thermophysical Problems in the Field of Nanoelectronics. *Russ Microelectron* **52**(8), 798–804 (2023) <https://doi.org/10.1134/S1063739723080115>
- [38] Saito, R., Dresselhaus, G., Dresselhaus, M.S.: Physical Properties of Carbon Nanotubes, Repr edn. Imperial College Press, London (1998)
- [39] Zimmermann, J., Pavone, P., Cuniberti, G.: Vibrational modes and low-temperature thermal properties of graphene and carbon nanotubes: Minimal force-constant model. *Phys. Rev. B* **78**(4), 045410 (2008) <https://doi.org/10.1103/PhysRevB.78.045410>
- [40] Mohr, M., Maultzsch, J., Dobardžić, E., Reich, S., Milošević, I., Damnjanović, M., Bosak, A., Krisch, M., Thomsen, C.: Phonon dispersion of graphite by inelastic x-ray scattering. *Phys. Rev. B* **76**(3), 035439 (2007) <https://doi.org/10.1103/PhysRevB.76.035439>
- [41] Liu, B., Johnson, S.G., Joannopoulos, J.D., Lu, L.: Generalized Gilat-Raubenheimer method for density-of-states calculation in photonic crystals. *J. Opt.* **20**(4), 044005 (2018) <https://doi.org/10.1088/2040-8986/aaaе52>
- [42] Gilat, G., Raubenheimer, L.J.: Accurate Numerical Method for Calculating Frequency-Distribution Functions in Solids. *Phys. Rev.* **144**(2), 390–395 (1966) <https://doi.org/10.1103/PhysRev.144.390>
- [43] Kaviany, M.: Heat Transfer Physics. CAMBRIDGE UNIVERSITY PRESS, Cambridge, New York (2008)
- [44] Srivastava, G.P.: The Physics of Phonons, 2nd edn. CRC Press, Boca Raton (2022). <https://doi.org/10.1201/9781003141273>
- [45] Ma, J., Li, W., Luo, X.: Examining the Callaway model for lattice thermal conductivity. *Phys. Rev. B* **90**(3), 035203 (2014) <https://doi.org/10.1103/PhysRevB.90.035203>
- [46] Mingo, N., Stewart, D.A., Broido, D.A., Lindsay, L., Li, W.: Ab Initio Thermal Transport. In: Shindé, S.L., Srivastava, G.P. (eds.) Length-Scale Dependent Phonon Interactions. Topics in Applied Physics, pp. 137–173. Springer, New York,

- NY (2014). https://doi.org/10.1007/978-1-4614-8651-0_5
- [47] Debye, P.: Zur Theorie der spezifischen Wärmen. Annalen der Physik **344**(14), 789–839 (1912) <https://doi.org/10.1002/andp.19123441404>
- [48] Mann, S., Rani, P., Kumar, R., Dubey, G.S., Jindal, V.K.: Thermodynamic properties of pure and doped (B, N) graphene. RSC Adv. **6**(15), 12158–12168 (2016) <https://doi.org/10.1039/C5RA25239C>
- [49] Huang, M.-J., Chang, T.-M., Liu, C.-K., Yu, C.-K.: A theoretical study of the specific heat and Debye temperature of low-dimensional materials. International Journal of Heat and Mass Transfer **51**(17), 4470–4479 (2008) <https://doi.org/10.1016/j.ijheatmasstransfer.2008.02.007>
- [50] McNamara, A.J., Lee, B.J., Zhang, Z.M.: Quantum Size Effect on the Lattice Specific Heat of Nanostructures. Nanoscale and Microscale Thermophysical Engineering **14**(1), 1–20 (2010) <https://doi.org/10.1080/15567260903468612>